Cement and Concrete Research 40 (2010) 740–751

Contents lists available at ScienceDirect

Cement and Concrete Research

journal homepage: http://ees.elsevier.com/CEMCON/default.asp

# Pore size and shape in mortar by thermoporometry

Zhenhua Sun, George W. Scherer *

*Princeton University, Civil & Env. Eng./PRISM, Eng. Quad. E-319, Princeton, NJ 08544, USA*

ARTICLE INFO

*Article history:*
Received 28 September 2009
Accepted 23 November 2009

*Keywords:*
Mercury porosimetry (B)
Microstructure (B)
Pore size distribution (B)
Thermodynamic calculations (B)
Freezing and thawing (C)

ABSTRACT

The pore structure of mortar (w/c = 0.55) was examined using thermoporometry (TPM), nitrogen adsorption/desorption (NAD), and mercury intrusion porosimetry (MIP). The TPM measurements were calibrated by comparison to NAD and MIP measurements on porous glass; similar comparisons were made on dried and resaturated mortars. For undried mortars, TPM provides the size of pore entries (from the freezing cycle) and interiors (from the melting cycle). In keeping with previous studies, we find that there is an unfrozen layer of water between the ice and the pore wall in porous glass that is about 0.8 nm thick; when lime-saturated water is used, the thickness of that layer increases by about 10%. In mortar, the unfrozen layer is about 1.0–1.2 nm thick, so no freezing occurs in pores with diameters ≤4.5 nm, at least down to −40 °C (where the radius of the crystal/liquid interface is ~1.5 nm). Based on the hysteresis in the freezing and melting curves, the larger mesopores in mortar were found to be rather spheroidal, while the smaller ones were more cylindrical.



## 1. Introduction

In the present study, we focus on the features of the pore network that are most relevant to frost damage in mortar and concrete: (i) the nanometric mesopores where large crystallization pressures can be generated and (ii) the macroscopic entrained air voids that provide protection [1]. The results presented here have been used to analyze the stress and strain in mortar during freezing [2].

The mass transport properties and the durability of cementitious materials are controlled by their pore structure, so considerable effort has been invested in characterization of the pore size distribution. The pores include molecular-scale interlayer spaces, nanometric "gel pores" between the primary particles of calcium-silicate-hydrate (C-S-H) [3], micrometric "capillary pores" that are remnants of the interstitial spaces between the unhydrated cement grains [4], deliberately entrained air voids with diameters on the order of 50–100 μm for frost protection [5,6], and entrapped air that can reach the millimeter scale in concrete [7]. The pore space is fully interconnected, as indicated by the fact that the liquid can be fully exchanged by solvents [8]; the definition of a pore size or shape is thus quite arbitrary, because there is actually only one pore with a complicated shape.

Every available method for characterizing pore structure has been applied to cement paste [8,9]. The low permeability of mature paste indicates that the transport properties are dominated by mesopores [10] (*i.e.*, those with diameters between 2 and 50 nm, according to the IUPAC definition), so extensive use has been made of nitrogen adsorption/desorption (NAD). An advantage of NAD is that the adsorption curve reveals the size of the pore interiors, while the desorption curve indicates the pore entry sizes, as long as they are in the mesopore range [11]. This means that capillary pores and larger voids are not measured, although their presence is detected, because the adsorbed volume is less than the total pore volume (which can be determined separately from density measurements). Mercury intrusion porosimetry (MIP) is capable in principle of measuring micron-scale pores, but it does not detect them in cement paste, because the large pores can only be entered through the mesopores; therefore, the porosimeter attributes the volume of a macropore to the size of its largest entrance. This has led to doubt about the validity of MIP data [12]. On the other hand, optical and scanning electron microscopy clearly reveal the size and amount of the larger pores [12], but are unable to resolve the mesopores [13], so the information is not sufficient for predicting transport behavior or freezing stresses.

A major disadvantage of NAD, MIP, and conventional scanning electron microscopy (SEM) is that the sample must be dried, and this results in significant alteration of the smaller pores [14–16]. The magnitude of the change in cement paste was demonstrated by Villadsen [17], who compared the pore size distributions found from MIP, NAD, and thermoporometry (TPM); moreover, he compared MIP samples dried following methanol exchange, and he performed TPM on samples that had been dried and resaturated. His results, some of which were presented in Ref. [10], clearly show that drying increases the pore volume and pore size compared to that of an undried sample. Environmental SEM avoids this problem, but cannot resolve the mesopores. Scattering of X-rays or neutrons can be performed on wet samples, but cannot provide a size distribution for the pores. A very powerful method for characterizing the pores in a wet sample is NMR

* Corresponding author.
*E-mail address:* scherer@princeton.edu (G.W. Scherer).

0008-8846/$ – see front matter © 2009 Elsevier Ltd. All rights reserved.
doi:10.1016/j.cemconres.2009.11.011

relaxation time analysis [18,19]. Since the spin relaxation time is slower for a molecule in bulk liquid than for one near a pore wall, proton NMR can determine the surface-to-volume ratio of a pore (comparable to the data from gas adsorption). Although NMR can be used to find the tortuosity of the pore space, it does not provide information about pore connectivity; that is, it does not indicate the fraction of the pore space that can be reached by passing through a pore of a given size.

Our goal is to measure the features controlling frost damage, which are macroscopic air voids and mesopores. The volume, size, and spacing of air voids are readily determined by optical microscopy. To quantify the size, shape, and connectivity of the mesopores, the most suitable methods are thermoporometry and cryoporometry. Both of these methods exploit the dependence of freezing temperature on pore size, but cryoporometry detects the phase transition using NMR [20,21], while TPM is done in a differential scanning calorimeter (DSC). The advantages of TPM and cryoporometry for freezing studies are that: (a) the sample remains saturated; (b) the stress that is exerted on the porous host by the ice is about 10 times less than that exerted by mercury in a pore of the same size [22]; (c) the amount of ice present at a given temperature is determined directly; and (d) the pore interior and the pore entry sizes are obtained. The disadvantages are that it is limited to mesopores with diameters larger than ~4 nm, because the pore liquid does not freeze in smaller pores, and it is not reliable for diameters larger than about 100 nm, because the freezing point depression is too small; moreover, the interpretation is complicated if there is solute in the pore liquid (as in cement paste) [23].

In this paper, we report the results of TPM performed on mortar, with the goal of predicting the stresses and strains developed during freezing. To perform the strain calculations, we must know the sizes and shapes of pores that are filled with ice as a function of temperature. The required data are most directly obtained calorimetrically, but the results depend on the thickness of the unfrozen layer of water that lies between the ice and the pore wall, and on the presence of solutes in the pore water. To quantify those effects, we compare pore size distributions obtained by mercury intrusion, nitrogen sorption, and thermoporometry on porous glass containing pure water or water saturated with calcium hydroxide (*i.e.,* limewater). Since the glass is not affected by the drying treatment, and is chemically inert, these experiments allow us to confirm the parameters (*viz.,* enthalpy of melting, crystal/liquid interfacial energy) used to interpret the calorimetric data, and to assess the effect of solute on the freezing behavior. The porous glass is subject to attack at high pH, so we retested it with pure water after the test with limewater to confirm that the microstructure was unchanged. Next, we examine dried mortar samples by nitrogen sorption, and compare the results to calorimetric measurements made on identical samples immediately after resaturation. This allows us to determine the thickness of the unfrozen layer of water in the pores of cement paste. Using those parameters, we measure the pore size distribution calorimetrically in a mortar that was never dried.

## 2. Thermoporometry

### 2.1. Thermodynamics

Thermoporometry is based on the fact that the freezing point of the pore liquid depends on the curvature of the crystal/liquid interface, $\kappa_{CL}$, according to the Gibbs–Thomson equation [1,24]:

$$\gamma_{CL}\kappa_{CL} = \int_T^{T_M(\infty)} \frac{(S_L - S_C)}{V_L}\, dT \tag{1}$$

where $\gamma_{CL}$ is the crystal/liquid interfacial energy, $S_L$ and $S_C$ are the molar entropies of the liquid and crystalline phases, $V_L$ is the molar volume of the liquid, and $T_M(\infty)$ is the melting temperature of a macroscopic crystal (*i.e.,* with effectively infinite radius). The Gibbs–Thomson equation was apparently first applied for pore size measurement by Kuhn et al. in a study of organic gels [25], and was independently proposed by Fagerlund in a study of cement paste [26]. However, the first rigorous development of the thermodynamic basis of thermoporometry was provided by Brun et al. [27] (BLQE), who pioneered the development of the technique. To extract the pore size distribution from our DSC data, we use the crystal/liquid surface energy and enthalpy data provided in Ref. [27]. However, there are some typographical errors and conceptual issues regarding that paper that are discussed in Sections 2.2 and 3.2.

The pore solution in cement paste includes calcium and alkali hydroxides with a total concentration on the order of half molar [28]. As ice forms in the pore, the solute is rejected by the ice crystals, so the concentration in the remaining liquid rises [23,29]. Elegant studies have been done to demonstrate the effect of pore size on the freezing of salt solutions [30], but we minimize the complications by replacing the pore solution with lime-saturated water, which is very dilute (~2 g $Ca(OH)_2$/liter of water). Tests using limewater in Vycor®, described in Section 4, demonstrate that reliable results are obtained by using the thermodynamic properties of water to interpret TPM data for samples containing limewater.

Suppose that a pore has an entry with radius $r_E$, but the interior (or, body) of the pore has radius $r_B$. The curvature of the crystal/liquid interface during freezing, $\kappa_F$, will depend on $r_E$, but the curvature during melting, $\kappa_M$, will be controlled by $r_B$. This results in a hysteresis in the melting and freezing temperatures. The shape parameter for the ice, λ, can be defined in terms of the curvatures or the undercoolings:

$$\lambda \equiv \frac{\kappa_M}{\kappa_F} = \int_{T_M(r_B-\delta)}^{T_M(\infty)} \Delta S_{fv}\, dT \Big/ \int_{T_M(r_E-\delta)}^{T_M(\infty)} \Delta S_{fv}\, dT \tag{2}$$

where $\Delta S_{fv} = (S_L - S_C)/V_L > 0$, $\delta$ is the thickness of the unfrozen layer of liquid against the pore wall, $T_M(r_E-\delta)$ is the melting point of ice with a radius of curvature sufficient to enter the pore, and $T_M(r_B-\delta)$ is the melting point of ice with the radius of curvature imposed by the interior of the pore body. We can find $\lambda(T)$ directly from the calorimetric data by evaluating Eq. (2), without any assumptions about pore shape. If the entropy of fusion is not a strong function of temperature, we can approximate λ by

$$\lambda \approx \frac{\Delta T_M}{\Delta T_F} = \frac{T_M(\infty) - T_M(r_B-\delta)}{T_M(\infty) - T_M(r_E-\delta)} \tag{3}$$

The quantity $\Delta T = T_M(\infty) - T$ is called the *undercooling*, and is positive at temperatures below the melting point of the macroscopic crystal. In Eq. (3), $\Delta T_M$ is the undercooling where melting occurs in a given pore and $\Delta T_F$ is the undercooling at which freezing occurs (*i.e.*, where the crystal/liquid interface enters the pore). Based on the data in BLQE [27], the integral of the entropy for pure water (in units of MPa) is

$$\int_T^{T_M} \Delta S_{fv} dT \approx -1.238T - 5.20 \times 10^{-3} T^2, \quad -40 \le T(^\circ C) \le 0 \tag{4}$$

A more precise estimate of λ can be obtained by using Eq. (4) in Eq. (2), but the result obtained from Eq. (3) is satisfactory [2]. This quantity is needed for calculating the stress exerted on the pore walls by ice during freezing, as explained in detail in Ref. [2].

The value of λ represents the pore shape only if the freezing and melting events occur in the same pore, which is not necessarily true. Consider the schematic calorimetric curves shown in Fig. 1. When the temperature drops to $T_F$, ice penetrates pore entries with radius $r_E$ which lead into pore interiors with a range of sizes, shown here as ranging from $r_{B1}$ to $r_{B3}$. During the melting cycle, the ice formed at $T_F$ will melt over a range of temperature from $T_{M1}$ to $T_{M3}$, reflecting the actual range of pore shapes. The smallest of the pore bodies frozen at $T_F$ (*viz.*, $r_{B3}$) will melt along with other small pores that were frozen at

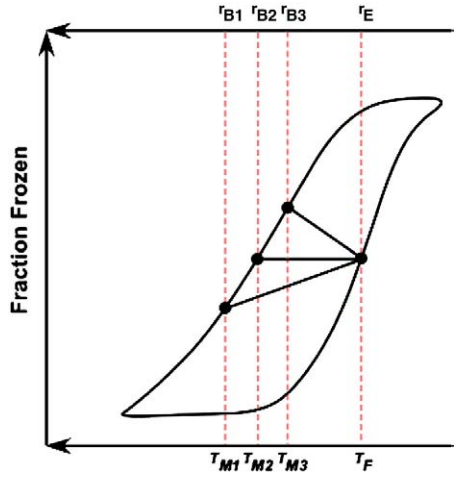


**Fig. 1.** Schematic calorimetric curves for freezing and melting cycles. During cooling, ice passes through a pore entry with radius $r_E$ at temperature $T_F$, and enters pore bodies with interior radii ranging from $r_{B1}$ to $r_{B3}$. During reheating, the ice in the pores melts at temperatures ranging from $T_{M1}$ to $T_{M3}$. We evaluate λ by comparing the undercoolings for melting and freezing at a constant fraction frozen, so in this case we use the undercoolings at $T_F$ and $T_{M2}$ to estimate the shape of all the pores entered at $T_F$.

lower temperatures (following penetration of pore entries smaller than $r_E$). Similarly, the ice that melts at any temperature will have been formed over a range of freezing temperatures. Since we have no way of knowing the actual pore shapes, we approximate the pore shape by assuming that all the ice formed at $T_F$ melts at $T_{M2}$, which corresponds to the same fraction of ice saturation (*i.e.*, the same volume fraction of the pore space occupied by ice) that was present at $T_F$. We could try to refine our approximation by running smaller temperature cycles. For example, we could cool to $T_F$ and then immediately reheat to see how closely the reheating curve follows the line from $T_F$ to $T_{M2}$. Of course, the reheating curve would fall below that line, because of the melting of the ice in pores with radius $r_{B3}$. In fact, such an experiment would not be enlightening, because it would indicate the size of the smaller pores entered at $T_F$ (*viz.*, those with interior radius $r_{B3}$), but would not reveal the existence of those with radii between $r_{B2}$ and $r_{B1}$. Our method should provide a good approximation for the average pore interior, $r_B$, corresponding to each pore entry size, $r_E$, as long as the distribution of $r_B$ corresponding to a given $r_E$ is reasonably consistent. For example, if the pores were all spheroidal and the interior sizes fell on a Gaussian distribution with a constant standard deviation, our method should provide a good average. In materials such as Vycor®, where the freezing and melting curves are steep, so that all the $r_{Bi}$ are similar, this method is particularly accurate. On the other hand, if there were an abrupt transition from spheroidal to cylindrical pore shapes in a certain size range, our estimate might be poor.

In the remainder of this paper, we will focus on finding the pore size distribution, which requires interpreting the curvatures in terms of pore radii, based on a model of pore shape.

### 2.2. Pore shape and hysteresis

To interpret the calorimetric data in terms of pore size, some assumptions must be made. In the analysis of NAD and MIP, it is typically assumed that the pores are cylinders, although for some materials it is more appropriate to approximate the pores as spheres or slits. Similarly, it is typical to interpret TPM data by assuming that the pores are cylindrical, so that ice growing into a pore has a hemispherical surface. The radius of the ice is smaller than that of the pore, because of the presence of a layer of water with thickness $\delta$ that does not freeze. Thus, the radius of curvature of the advancing hemispherical interface is $r_p-\delta$, and the curvature of the interface is $\kappa_F=2/(r_p-\delta)$. After the ice has filled the pore, it takes on a cylindrical shape, so BLQE argue that it melts at a temperature corresponding to the curvature of the side of the cylinder, $\kappa_M=1/(r_p-\delta)$. From Eq. (1), we see that the temperature of the phase transition is approximately related to the curvature of the crystal by

$$\Delta T \approx \frac{\gamma_{CL}\kappa_{CL}}{\Delta S_{fv}} \tag{5}$$

so the cylindrical crystal will melt at an undercooling, $\Delta T_M$, that is half as large as that at which it froze, $\Delta T_F$. If the hysteresis in the TPM data is that large, BLQE conclude that the pores are cylindrical. However, if the pores are spheroidal, then the interior radius can be much larger than that of the pore entry, in which case the hysteresis will be greater than for a cylinder. Thus, the magnitude of the hysteresis provides a clue regarding the shape of the pores.

If the pores are assumed to be cylindrical, then a pore size distribution is imagined to resemble Fig. 2a, with abrupt changes in radius, followed by uniform circular cylindrical sections. In Fig. 2b, the undercooling is large enough to permit the ice to enter pore A, but not pore B; after further cooling, the ice will enter pore B, but be arrested at the entrance to the smaller pore C (Fig. 2c). Once $T$ is low enough to allow ice to enter C ($T=T_M-\Delta T_F^C$), it can also enter D, so they freeze at the same time (Fig. 2d). When the temperature is raised, the ice in pore C will melt first, at an undercooling of $\Delta T_M^C=\Delta T_F^C/2$, as shown in Fig. 3. According to BLQE, when the temperature rises to $T=T_M-\Delta T_F^B/2$, the ice in pores B and D will melt, and the ice in the largest pore will melt when $T=T_M-\Delta T_F^A/2$. Thus, pores B and D show different hysteresis because of the difference in their connectivity, rather than their size and shape. During the heating cycle, the first melting event indicates a hysteresis equal to the length of arrow ① in Fig. 3, which correctly represents the shape of pore C. Similarly, events ③ and ④ correctly reveal the shapes of pores A and B. Event ② shows a hysteresis greater than a factor of 2, as if the pore were spheroidal, which is not true for pore D; nevertheless, the result

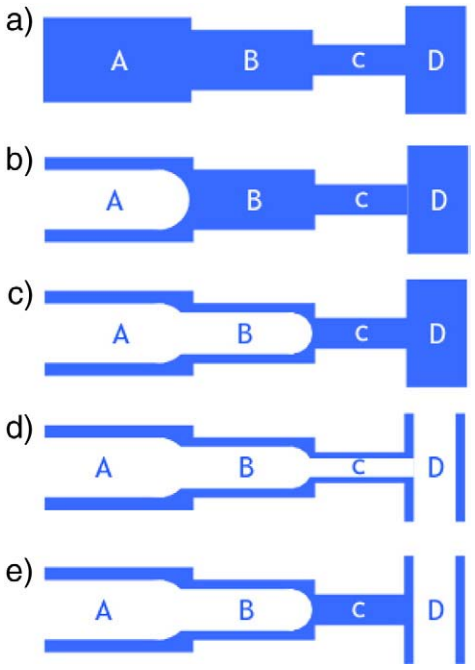


**Fig. 2.** a) Schematic of cylindrical pore distribution. b) $T$ is low enough for ice to enter pore A, but not pore B. c) $T$ is low enough for ice to enter pore B, but not C. d) When $T$ is low enough for ice to enter pore C, it can also enter pore D. e) During melting, the first ice to melt is in pore C, leaving a hemispherical interface in pore B and a cylindrical interface in pore D.

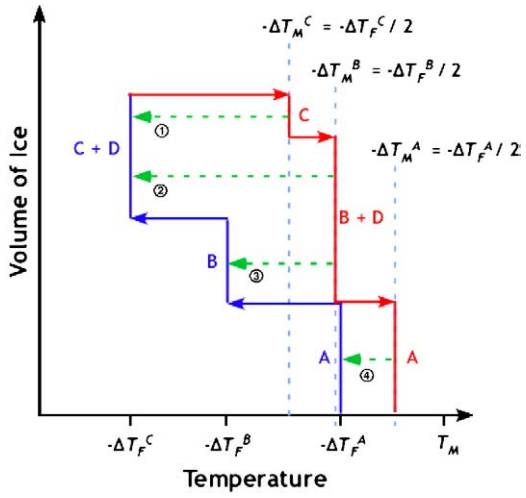


**Fig. 3.** Schematic of freeze/thaw hysteresis corresponding to the cylindrical pore network in Fig. 2, assuming that melting occurs from the side. The segments with arrows pointing to the left represent freezing, while those pointing right represent melting. For the ice in pores A, B, and C, melting occurs at an undercooling half as large as that at which ice entered those pores; however, for pore D, the hysteresis is larger, because ice entered by way of pore C, but melting occurs independently in each pore. The dashed arrows show the apparent hysteresis, as explained in the text.

correctly indicates that there is a large pore with a small entry, and provides a good approximation of the amount of ice in that pore.

Let us reconsider whether a filled pore will actually melt from the lateral surface or from the end. It may be reasonable to assume that the ice in pore C will melt at a temperature corresponding to a curvature of $1/(r_C-\delta)$, but it is less obvious what pores B and D will do. After pore C has melted, the water in the pore will be in equilibrium with a crystal/liquid interface having a curvature infinitesimally larger than $1/(r_C-\delta)$; thus, the ice in pore B will terminate in a hemispherical cap with radius $2(r_C-\delta)$ and curvature $2/[2(r_C-\delta)]$. Now, the ice in pore B will melt from the end if the temperature is in equilibrium with a curvature $<2/(r_B-\delta)$, so pores B and C will melt simultaneously unless $r_B-\delta>2(r_C-\delta)$. That is, the melting of pore C will lead to the melting of adjacent pores until the interface arrives at a pore twice as large as C. For that pore (let us suppose it is A, so $r_A=2r_C$), the curvature at the pore mouth is now $2/[2(r_C-\delta)]\approx 2/(r_A-2\delta)$, and the curvature of the side is $1/(r_A-\delta)$. As the temperature continues to increase, pore A will also melt from the end, because $2/(r_A-2\delta)>1/(r_A-\delta)$ for any $r_A>0$. Based on this reasoning, the only pores that will melt from their lateral surfaces are those which are connected at each end to pores more than twice as large. However, this is valid only for co-axial pores, such as A and C. Pore D is perpendicular to C, so the curvature of the ice in D is not altered by the melting of C (see Fig. 2e), and it will melt from the side at a temperature corresponding to a curvature of $1/(r_D-\delta)$. We conclude that the melting in cylindrical pores can occur at a temperature such that $\lambda=0.5$, if melting occurs from the side, or $\lambda\approx 1$, if melting occurs from the end, and the observed result depends on the connectivity of the pores. In the latter case, the hysteresis comes primarily from network effects, rather than pore shape (*e.g.*, C freezes at a lower temperature than B, but they melt together; B and D are the same size and shape, but they freeze and melt at different temperatures, because of the way they are connected to A and C).

If the actual pore system involves a sequence of constrictions between larger chambers, then a cylindrical network is not a very good model. An alternative would be the network of spherical pores sketched in Fig. 4, which allows for very large hysteresis, because large pores may have tiny entrances. The curvature during freezing is $\kappa_F=2/(r_E-\delta)$ and during melting $\kappa_M=2/(r_B-\delta)$, so Eq. (2) indicates that the shape factor $\lambda=(r_E-\delta)/(r_B-\delta)$, falls in the range $0<\lambda\leq 1$.

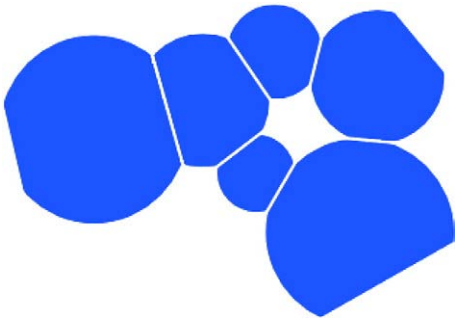

**Fig. 4.** Schematic illustration of spherical pore size distribution, where the white lines at intersections of the spheres show the diameters of the pore entries.

A different sort of spherical pore network was envisioned by BLQE. They point out that the radius of the critical nucleus for homogeneous nucleation, $r^*$, is given by an equation equivalent to Eq. (1) [31]:

$$\frac{2\gamma_{CL}}{r^*} = \int_T^{T_M(\infty)} \frac{(S_L-S_C)}{V_L}\,dT \approx \Delta S_{fv}\Delta T \tag{6}$$

That is, the critical nucleus is a crystal whose size is such that its melting point is equal to the current temperature; smaller crystals melt and larger ones grow. BLQE therefore proposed that a crystal would spontaneously appear in a pore with radius $r^*$ at its melting point. By assuming that such nucleation was probable, BLQE concluded that the shape factor for spherical pores would be $\lambda=1$, because freezing and melting would occur at the same temperature. That is, rather than requiring the ice to enter through a small entry, they assume that it can nucleate homogeneously in a pore with radius $r^*$ as soon as the temperature is low enough to satisfy Eq. (6). However, this is a misconception based on neglect of the kinetics of nucleation. As explained in detail in Ref. [32], the *rate* of homogeneous nucleation for water is only significant at temperatures on the order of −38 °C [33], where $r^*\approx 1.6$ nm, because it is unlikely for thermal fluctuations to create larger crystals; consequently, the probability of nucleation in any given mesopore is vanishingly small. Therefore, we will assume that ice can only enter a spherical pore by passing through an entry with a radius $r_E\leq r_B$.

We will use the cylindrical and spherical models to evaluate the TPM data for our mortars, since those models provide bounds on the expected pore shape in mortar and porous glass. For the cylindrical pore, we will allow for melting entirely from the side or entirely from the end.

## 3. Experimental procedure

### 3.1. Methods

The samples used in the present experiments were provided by Tremblay et al. (Laval University), who prepared the samples for the study of salt scaling presented in Ref. [34]. All mortars were made from ASTM Type I ordinary Portland cement. A low percentage (20% by volume) of Ottawa sand type C-109 was used as fine aggregate to improve mixture homogeneity. Mixtures were prepared at two water/binder ratios (0.40 and 0.55) and three different air contents (0, 3 and 6 vol%) using a synthetic detergent air-entraining agent (Microair by BASF). Batching was done using a counter-current pan mixer. A Welan gum-based viscosity modifying agent (VMA) was added at the end of the mixing sequence to minimize internal bleeding. The specimens were stored in a wet room at 100% RH and 23 °C from 24 h after mixing until they were sent to us (at an age of about 1.5 years); they had dried in transit, but were immersed in limewater (*i.e.*, water saturated with calcium hydroxide) in our lab until use (about 6 months).

To measure the porosity of the samples, the weights of both fully saturated and dried samples (0.5×3×3 cm) were measured. The samples were vacuum saturated by placing them in a desiccator and evacuating the vessel for 3 h, and then back-filling with water for another 2 h. The fully saturated samples were weighed and then dried in the oven at 105 °C for 2 days and weighed again; the pore volume of the sample was then calculated from the weight difference of wet and dry samples, assuming that the pore water has a density of 1.0 g/cm$^3$. This high temperature removes interlayer water [8] and may cause some dehydration of C-S-H or ettringite [35]. Our purpose is to find the volume of pore liquid that can exert pressure on the body during freezing, and it seems reasonable to exclude the interlayer water from that quantity, as argued by Ghabezloo et al. [36]. Therefore, we also used a milder drying treatment intended to remove water only from the capillary and gel pores. Mortars were exchanged into isopropanol and weighed after drying at 60 °C; the weight gain after resaturating with water was used to determine the porosity. To determine the skeletal density, mortars with 0 and 6% entrained air were measured by helium pycnometry (Micromeritics Accupyc 1330) after exchange into isopropanol and drying at 60 °C for 2 weeks.

Mortar samples were examined by TPM, MIP, and NAD. To minimize the difference in the pore size distributions obtained by these methods, the samples were subjected to the same preparation procedure. The limewater saturated mortar was immersed in isopropanol for 12 h to replace the water in the pores with alcohol, then dried in an oven at 60 °C for 12 h; after that, the DSC samples were vacuum saturated with water, as described above for porosity measurements. We assume that some calcium hydroxide in the paste dissolves in the water, so that the pore liquid is equivalent to limewater. To maximize the sensitivity, samples were cut in the form of disks ~5×5×1 mm thick to fill the DSC pan. A drop of kerosene was added on top of the sample to improve thermal contact with the aluminum sample pan and to minimize drying of the sample while the lid was being crimped onto the pan. This procedure, together with the small sample size, minimizes the temperature lag between the instrument and the sample that has been reported with much larger samples [23]. The temperature cycles ranged from +5 °C to about −60 °C at a rate of 0.25 °C/min using a Perkin Elmer Differential Scanning Calorimeter (Pyris 1), which had been calibrated using pure water and decane. The accuracy of the temperature measurement is ±0.1 °C and that of the enthalpy is ±2%. The baseline heat flow changes as the pore liquid freezes, because it depends on the heat capacities of the ice and water, and the amounts of those phases are changing. The scheme for calculating the baseline is explained in Appendix 1.

Bulk water can be cooled below 0 °C without freezing, owing to the energetic barrier to nucleation, and this effect must not be confused with the effect of pore size on freezing temperature. Therefore, to determine the pore size distribution by TPM, it is essential to cool the sample until some of the pore liquid freezes, then to heat to a temperature just below the melting point. The first freezing cycle creates crystals that reside in macropores or on the exterior surface of the sample; during reheating, the smaller crystals in mesopores melt, but the macroscopic ice persists and these crystals propagate through the pores as the temperature is decreased again. The pore entry radius is then found from the second (and subsequent) freezing cycles, while the size of the pore interior is found from the first (and subsequent) melting cycles, all of which are performed without heating above $T_M(\infty)$. In our experiments, the first cooling cycle descended to −20 °C, and the maximum temperature on all but the last heating cycles was about −0.05 °C.

The interpretation of TPM data for mortar is complicated by the presence of solutes in the pore water. Since our samples (~2×3×10 cm) were stored for an extended period in a large volume (~48 liters) of limewater, the alkali are likely to have diffused out, so the pores are expected to contain a solution very similar to limewater. To evaluate the effect of the solute on the freezing curve, a sample of Vycor® glass was studied by NAD and by TPM with either pure water or limewater in the pores. That sample was cut into a plate about 4×4×1 mm; it was covered with a drop of kerosene to avoid evaporation, and was subjected to heating and cooling cycles over the range from +5 to −35 °C at a rate of 0.25 °C/min. To determine whether the glass was altered by the basic limewater (pH = 12.5), the sample was resaturated with pure water and the TPM measurements were repeated.

The use of mercury intrusion for measuring the pore size of cementitious materials is problematic, because drying is known to alter the microstructure (*e.g.*, the permeability rises by two orders of magnitude, apparently as a result of microcracking [14]); moreover, the pressure exerted during intrusion can cause damage [37]. The samples prepared for the salt scaling tests had been dried in transit, so the drying damage was largely done before our tests began. However, some of that damage is likely to have healed by hydration during lengthy storage (several months) in limewater. Before MIP measurements, the water-saturated samples were exchanged in isopropanol, and then dried at 60 °C. MIP was performed using a Micromeritics 9410 on granules ~2 mm in diameter. One measurement was made shortly after the samples were obtained, and another about a year later (contemporaneously with the DSC measurements). As reported in the next section, a significant decrease in pore volume resulted from the year of aging in limewater, so we compare the DSC results to the later MIP data. This means that the pore structure of our samples is different from that of the younger samples used in the scaling study [34]; however, the samples measured in this study by NAD and DSC were strictly equivalent.

### 3.2. Interpretation of TPM data

To analyze the TPM data, we follow the procedure suggested by BLQE [27]. The DSC reports the rate of heat exchange with the sample, which is proportional to the amount of ice that melts or freezes. To find the amount of pore volume occupied by ice, it is necessary to know the heat of fusion of ice in the mesopores, which is quite different from that of bulk ice. BLQE recognized that external water, or water expelled from the sample during freezing, provides a layer of ice on the outer surface which is in equilibrium with the surrounding vapor. If the ice remains in thermodynamic equilibrium with the atmosphere and with the water in the pores, then the liquid must be under negative pressure. That is, the convex surface of the ice that penetrates the pores creates a positive pressure inside the ice that must be balanced by suction in the water, if the internal pressure of the ice is to remain atmospheric. This is discussed in detail in Ref. [1] in connection with Fig. 4 of that paper. Using the thermal properties of water and ice, BLQE calculate the heat exchange per gram of water at temperature $T$, $W_{th}$, taking account of the temperature dependence of the heat capacities of water and ice, and the effect of capillary suction in the pore liquid. The result is their Eq. (13), which differs significantly from the heat of fusion used by other authors [38–40], owing to inclusion of the effect of pore pressure. BLQE add another correction (derived in Ref. [41]) to take account of the effect of the crystal/liquid surface area created when ice forms in a pore. This is a large correction that is usually neglected in the analysis of TPM, perhaps because the derivation is not available in English, so it is explained in Appendix 2. When ice in a pore is melted, the energy of the interface is liberated, so it constitutes a positive contribution to the heat of fusion whose magnitude depends on the area of the crystal/liquid interface. During freezing, when the advancing interface is roughly hemispherical with $\kappa_F = 2/(r_p - \delta)$, the correction, given by BLQE's Eq. (9), is so large that it almost exactly offsets the temperature dependence of $W_{th}$. The corrected heat of fusion during freezing is

$$W'_{th}\,(\mathrm{J/g}) \approx 332.4 \text{ (freezing)} \tag{7}$$

and varies by <0.6% over $-40 < T\,(^\circ\mathrm{C}) < 0$. During melting, when the curvature of the interface in a cylindrical pore would be half as large, the correction significantly reduces, but does not eliminate, the temperature dependence of $W'_{th}$. For melting from the side of a

cylindrical pore, the result is found by halving the correction term in BLQE's Eq. (9). The result is given with a relative error<0.25% by

$$W'_{th}(T)\ (\mathrm{J/g}) \approx 333.8 + 1.797\,[T - T_M\ (\infty)]\ \ (\mathrm{Melting,\ Cylinder}) \quad (8)$$

For melting in a spherical pore, or in a cylindrical pore melting from the end, Eq. (7) should be used. Dividing the measured heat release by Eqs. (7) or (8), the mass of ice formed or melted in each temperature interval is found; the volume of ice, $v_{ice}$, is obtained by dividing by the density of ice [42], which is described by

$$\rho_{ice}\,(\mathrm{g/cm^3}) \approx 0.9167 - 2.053\times10^{-4}T - 1.357\times10^{-6}T^2 \quad (9)$$

where $T$ is in degrees Celsius. It is incorrect to use the density of water to analyze the freezing curve, and the density of ice for the melting curve, as is done by some authors [38–40]. The quantity of interest is the volume of the pore space that is filled with ice during freezing, or freed of ice during melting, so in either case it is the density of ice that is relevant. Rather than using these equations for $W'_{th}$, BLQE introduce an apparent heat of fusion that is related to $W'_{th}$ by

$$W_a = W'_{th}\left(\frac{r_{CL}}{r_{CL}+\delta}\right)^n \quad (10)$$

where $n=2$ for a cylindrical pore and $n=3$ for a spherical pore. Dividing the measured heat released by $W_a$ yields the volume of the pore, rather than the volume of ice formed during each temperature interval. In the present analysis, we do not use this approach, because we don't yet know $\delta$ for our samples.

The radius of the crystal/liquid interface, $r_{CL}$, is given by Eq. (6) of Ref. [27] as

$$\frac{2\gamma_{CL}}{r_{CL}} = \int_T^{T_M(\infty)} \Delta S_{fv}\,dT \quad (11)$$

which is obtained from Eq. (1) by assuming that the advancing interface is hemispherical, so that $\kappa_C = 2/r_{CL}$. To evaluate Eq. (11), it is necessary to know $\gamma_{CL}$. BLQE performed a series of measurements on samples with narrow pore size distributions and found the surface energy that would bring their TPM results into agreement with MIP measurements. Their results, shown in Fig. 5, were fit to the following equation, which is their Eq. (17):

$$\gamma_{CL}(\mathrm{J/m^2}) = 0.0409 + 3.9\times10^{-4}(T - T_M) \quad (12)$$

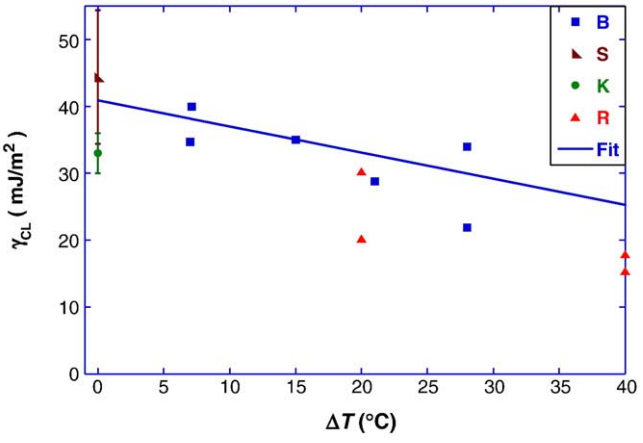


**Fig. 5.** Crystal/liquid interfacial energies measured by Brun et al. [27] by calibrating TPM against MIP (B); by Skapski et al. [43] from the curvature of ice in a tapered capillary (S); by Ketcham and Hobbs [44] from grain boundary angles (K); by Rasmussen and MacKenzie [33] from homogeneous nucleation temperatures.

At $T \approx T_M = 0$ °C, Eq. (12) is in reasonable agreement with the value found by Skapski et al. [43] by measuring the curvature of a crystal in a tapered capillary at temperatures near the melting point; it is slightly higher than the value obtained by Ketcham and Hobbs [44] from grain boundary angles in ice. The predictions of Eq. (12) at lower temperatures are significantly higher than those inferred by Rasmussen and MacKenzie [33] from the temperature of homogeneous nucleation of ice. BLQE plausibly excuse this discrepancy by arguing that the assumptions of nucleation theory, including the assumed shape of the nucleus, add uncertainty to the value of $\gamma_{CL}$. An issue that has not been addressed in the context of TPM is the anisotropy of the surface energy of ice. There is even dispute about the phase of ice that appears in small pores, where some studies suggest that cubic ice forms [45,46], while others find hexagonal ice [47,48]. These uncertainties may contribute to the scatter of values found in the literature. The values extracted from TPM data by Ishikiriyama et al. [38] are even lower than those found from homogeneous nucleation; moreover, they obtained the unphysical result that $\gamma_{CL}$ was different at a given temperature during the cooling and heating cycles. Their data are compromised, because their fitting involved the uncorrected heat of fusion of bulk water, and they used the density of water, rather than ice, to evaluate the freezing cycle. Based on the data in Fig. 5, we feel that it is most reasonable to use Eq. (12) for $\gamma_{CL}$, since it is obtained from TPM experiments using the best thermodynamic data.

Using BLQE's Eq. (13) for $(S_L - S_C)$ with data from Lange's handbook [49] for the specific volume of water, we evaluated Eq. (11) numerically, and fit the result to a parabolic expression in $T$. Inverting that expression gives an equation for $T$ as a function of $\gamma_{CL}/r_{CL}$; comparison to Eq. (16) of Ref. [27] reveals a typographical error: the factor of $10^{-4}$ in the first term of that equation should be $10^{+4}$. With this correction, and using Eq. (12) for $\gamma_{CL}$, we obtain an expression for $r_{CL}$ as a function of $T$ that can be fit to a hyperbolic form. There is an unfrozen layer of water with thickness $\delta$, so the radius of the pore, $r_p$, is related to the radius of the ice crystal by $r_p = r_{CL} + \delta$. For water, the result is

$$r_p(\mathrm{nm}) = \frac{64.67}{\Delta T} - 0.23 + \delta\ \ (\mathrm{water,\ freezing}) \quad (13)$$

Based on comparisons to MIP and TPM results for various porous materials, BLQE concluded that $\delta = 0.8$ nm for water. The final result is Eq. (19) of Ref. [27], which relates the pore radius to the undercooling during freezing:

$$r_p(\mathrm{nm}) = \frac{64.67}{\Delta T} + 0.57\ \ (\mathrm{water,\ freezing,\ }\delta = 0.8\ \mathrm{nm}) \quad (14)$$

During freezing, the amount of heat released at temperature $T$ indicates the volume of pores that are accessible through entries with radius $r_p$ given by Eqs. (13) or (14).

The radius of the pore that the ice enters is $r_p = r_{CL} + \delta$; therefore, the volume of the pores in which freezing occurs, $v_{pore}$, is greater than the volume of the ice by a factor of

$$v_{pore} = v_{ice}\left(\frac{r_{CL}+\delta}{r_{CL}}\right)^n = v_{ice}\left(\frac{r_B}{r_B - \delta}\right)^n \quad (15)$$

where $n=2$ for a cylindrical pore and $n=3$ for a spherical pore. To find the unfrozen layer thickness requires fitting of the melting curve (which depends on the pore interior radius), and finding $\delta$ such that the total pore volume is the same as that found by nitrogen sorption. The volume comparison should include only the pores that the ice can enter, which means that the NAD pore volume that is relevant is the volume in pores larger than

$$r_{\min} = \delta + \frac{2}{\kappa_F(T_{\min})} \approx \delta + \frac{2\gamma_{CL}}{\Delta S_{fv}(T_M(\infty) - T_{\min})} \quad (16)$$

where $T_{min}$ is the lowest temperature of the TPM experiment; the approximation follows from Eq. (5). To find $\delta$ for the mortar, a calibration experiment was performed in which a sample of mortar was dried (at 60 °C, following exchange into isopropanol) and analyzed by NAD, and then resaturated with water and measured using TPM. The measured pore volumes were brought into agreement by iteratively adjusting $\delta$. Once $\delta$ is known from that type of experiment, the same value can be used for other mortars, so it is not necessary to combine TPM and NAD routinely. Evidently, TPM cannot analyze pores smaller than $r_{min}$, but the volume of pores smaller than $r_{min}$ can be found by measuring the weight loss of the sample on drying, and comparing that to the measured pore volume.

## 4. Results

The porosity and density values for the mortars are shown in Table 1. An upper bound on the porosity, $\phi$, is found from the weight loss upon heating to 105 °C. Dividing the bulk density by $1-\phi$ yields a skeletal density of $2430\pm30$ kg/m$^3$, but this is an overestimate; the values from helium pycnometry are about 4% lower. For the sample without air entrainment, given the bulk density ($\rho_b=1.681$ g/cm$^3$) and the skeletal density from pycnometry ($\rho_s=2.318$ g/cm$^3$), the pore volume is $V_p=1/\rho_b-1/\rho_s=0.164$ cm$^3$/g, and the porosity is $\phi=1-\rho_b/\rho_s=0.275$. The values of air content in the mortars that were measured in Ref. [34] are shown in the table, along with values estimated from the ratios of the bulk densities of the dry samples, and they are seen to be consistent. The ratios of the saturated densities show that the sample with a nominal air content of 3% has a density 2% lower than the sample without air entrainment, so the air voids are largely empty. The sample with a nominal air content of 6% has a saturated density 5.5% lower than sample without AEA, so its voids are also empty. After the non-air-entrained mortar was exchanged into alcohol and dried at 60 °C, it was resaturated with water; the weight gain corresponded to a pore volume of 0.161 ml/g, which agrees well with the value calculated from the pycnometry data.

Fig. 6 shows a comparison of DSC data from three melting and freezing cycles for mortar samples; two have no air entrainment, and one contains 6% air. The agreement is quite good, showing that the data are reproducible, and that air entrainment has little effect on the size of the mesopores. The amount of ice detected during melting and freezing is typically constant within ~3%, as shown in Table 2. One sample was overheated during the first melting cycle, so macroscopic ice melted, and heterogeneous nucleation of ice occurred abruptly at about −2 °C during the subsequent freezing cycle; therefore, the portion of the curve at higher temperatures contains no information about the pore size. Nevertheless, the portion at lower temperatures agrees with the curves for samples that were not overheated, in which ice propagated from the pre-existing nuclei. The undercoolings during melting and freezing are indicated at the (arbitrarily chosen) point

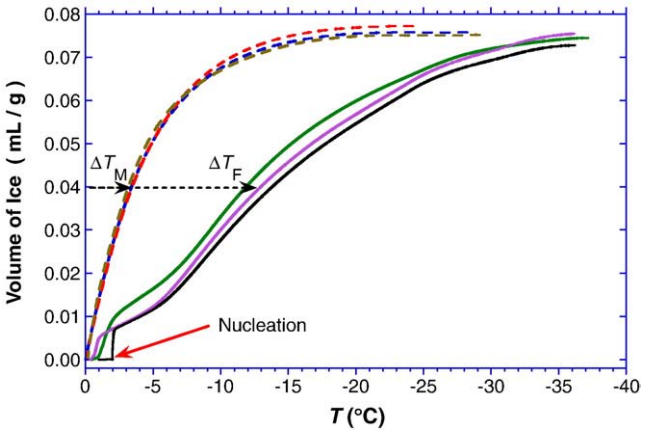


**Fig. 6.** Volume of ice in mortar versus temperature during freezing (solid curves) and melting (dashed curves); the left-most curve in each group has 6% entrained air, and the others have none. The undercoolings during the freezing ($\Delta T_F$) and melting ($\Delta T_M$) cycles are indicated for an ice content of 0.04 ml ice/g of dry mortar. One sample was overheated during the first melting cycle, so ice suddenly nucleated at about −2 °C during the subsequent freezing cycle (labeled "Nucleation"); the rest of the curve is not significantly affected.

where the sample contains 0.04 ml of ice per gram of dry mortar. The ratio of these undercoolings is a measure of the pore shape. Using pairs of values found in this way, the shape parameter λ is calculated from Eqs. (2) and (4), with the results shown in Fig. 7.

For the mortar, Fig. 7 shows that $\lambda<0.5$, so the pores are spheroidal, rather than cylindrical. The value of λ shoots up when the volume fraction of ice, $\phi_C$, is high or low, but this is an artifact. For example, the melting curves in Fig. 6 are almost horizontal below −15 °C, and the same is true of the freezing curves below about −30 °C. This leads to large uncertainties in the ratio of the undercoolings for $\phi_C>0.9$. Similarly, there are uncertainties in the part of the curve near the melting point, where the temperature cycle reverses. Consequently, we have truncated the plot for $\phi_C<0.1$ and $\phi_C>0.9$. The shape factor for the porous glass is always >0.5, indicating that the pores are roughly cylindrical, but the ice in a significant fraction of the pores melts from the end owing to network (connectivity) effects. However, most melting clearly occurs from the sides of the cylindrical pores, since otherwise we would find $\lambda\approx1$.

To extract the pore size distributions from the TPM data, we need to know the thickness of the unfrozen layer, $\delta$. This was found for each model by forcing the pore volumes to agree with those obtained from NAD. The calculation must be done iteratively, because the comparison should include only the portion of the distribution that the ice can enter at the lowest temperature of the cycle, but as indicated in Eq. (16) the bounding radius, $r_{min}$, depends on $\delta$. The results of the calculations are summarized in Table 3. For pure water in Vycor®, we find $\delta=0.74$ nm for cylindrical pores that melt from the side, and $\delta=0.96$ nm for spherical pores; this is in reasonable agreement with the value $\delta=0.8$ nm found by BLQE using the same models. A larger value is found from the model in which melting is assumed to occur from the end of the cylinder, because that model does not give a realistic representation of the process (as demonstrated by the magnitude of the hysteresis). When the porous glass is saturated with limewater, the layer thickness is found to be slightly larger, but

**Table 1**
Density and porosity of mortar (w/c = 0.55).

| | | | |
|---|---|---|---|
| Air content[a] | 0 (1.5) [0] | 3 (5.0) [4.0] | 6 (5.8) [6.0] |
| Saturated density[b] (kg/m$^3$) | 1993 | 1953 | 1884 |
| Bulk density[c] (kg/m$^3$) | 1681 | 1614 | 1517 |
| Skeletal density[d] (kg/m$^3$) | 2443 (2498) [2318] | 2442 (2642) | 2397 (2638) [2313] |
| Porosity[e] | 0.312 (0.268) | 0.339 | 0.367 (0.333) |

[a] Nominal air content (Measured value from Ref. [34]) [Calculated from ratio of dry bulk densities].
[b] Sample saturated, except for air voids.
[c] Calculated from initial volume and weight after drying at 105 °C.
[d] Calculated from bulk density and porosity (Calculated from bulk density and porosity, allowing for measured volume of air voids) [From helium pycnometry].
[e] Calculated from weight loss at 105 °C (after drying at 60 °C).

**Table 2**
Volume of ice detected in mortar by DSC (for the samples shown in Fig. 6).

| Cycle | Freezing (ml/g) | Melting (ml/g) |
|---|---|---|
| 1 | 0.0772 | 0.0757 |
| 2 | 0.0755 | 0.0745 |
| 3 | 0.0751 | 0.0728 |

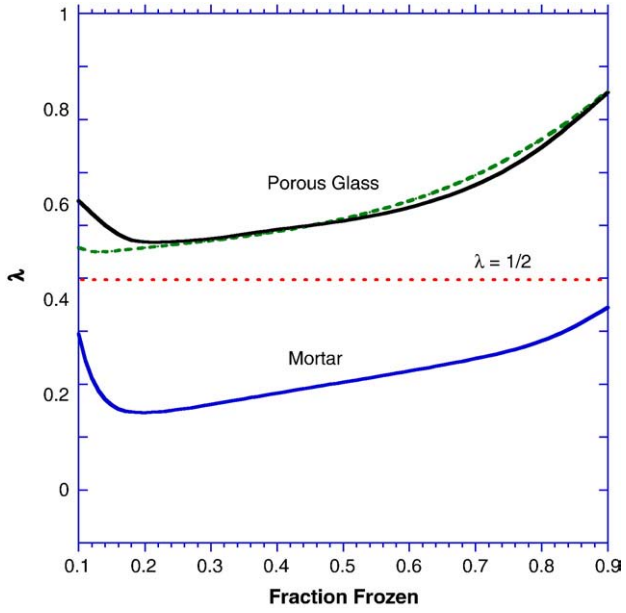


**Fig. 7.** Shape factor, λ, defined in Eq. (2), for porous glass saturated with pure water (solid curve) or limewater (dashed curve) and mortar saturated with limewater. The dotted line indicates the value (λ = ½) expected for perfect cylinders where melting occurs exclusively from the side. The abscissa is the fraction of the pore volume that contains ice (*i.e.*, the degree of saturation of the pore space with ice).

the difference is probably smaller than the uncertainty in the calculation. The DSC curves for Vycor® saturated with pure water and limewater are compared in Fig. 8. In the mortar, the unfrozen layer is found to be consistently larger than in porous glass, even when the glass contains limewater. Given the relatively low value of λ indicated for the mortar in Fig. 7, the spheroidal model is probably the most appropriate model, and it yields $\delta = 1.2$ nm.

The pore size distributions obtained for porous glass by NAD are compared with the TPM results in Fig. 9. The desorption curve is expected to correspond to the freezing curve, since both are interpreted by assuming that a hemispherical meniscus, which is concave toward the non-wetting phase, penetrates the pore opening. As shown in Fig. 9a, the peak of the NAD distribution is only about 0.6 nm to the left of the TPM distributions. The latter are only slightly shifted relative to one another by an amount related to the corresponding value of δ. The differences are greater in Fig. 9b, where the adsorption and melting data are compared. The adsorption curve falls between those for cylinders with melting from the side or end, but is closer to the former, which is consistent with the value of λ shown in Fig. 7. The pore volume of the Vycor® is 0.252 ml/g.

The pore size distributions from NAD for dried mortar samples are compared with TPM results for resaturated samples in Fig. 10. The NAD curves extend to pores with entry radii of 1.25 nm, whereas the smallest pore radius entered by ice at −40 °C is about 2.5 nm, according to Table 3. Fig. 7 indicates that $0.25 \le \lambda \le 0.45$ for the mortar, so the pores are roughly cylindrical, but the pore interiors are

**Table 3**
Unfrozen water layer thickness, δ, and radius of the smallest pore entered during freezing cycle, $r_{min}$.

| Pore model | Vycor® pure water | | Vycor® limewater | | Mortar limewater | |
|---|---|---|---|---|---|---|
| | δ (nm) | $r_{min}$ (nm) | δ (nm) | $r_{min}$ (nm) | δ (nm) | $r_{min}$ (nm) |
| Cylinder (Melt side) | 0.67 | 2.1 | 0.74 | 2.6 | 0.98 | 2.4 |
| Cylinder (Melt end) | 1.2 | 2.8 | 1.4 | 3.3 | 1.6 | 3.0 |
| Sphere | 0.96 | 2.3 | 1.0 | 2.9 | 1.2 | 2.6 |

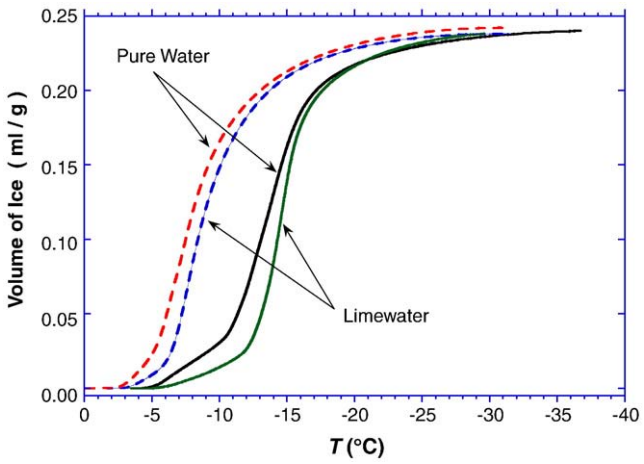


**Fig. 8.** Volume of ice in Vycor® versus temperature during freezing (solid curves) and melting (dashed curves), for samples saturated with pure water and limewater.

somewhat larger than the entries, particularly for the larger pores. The most accurate representation of the pore size distribution should lie between those for the cylindrical pore melting from the side and the spherical pore.

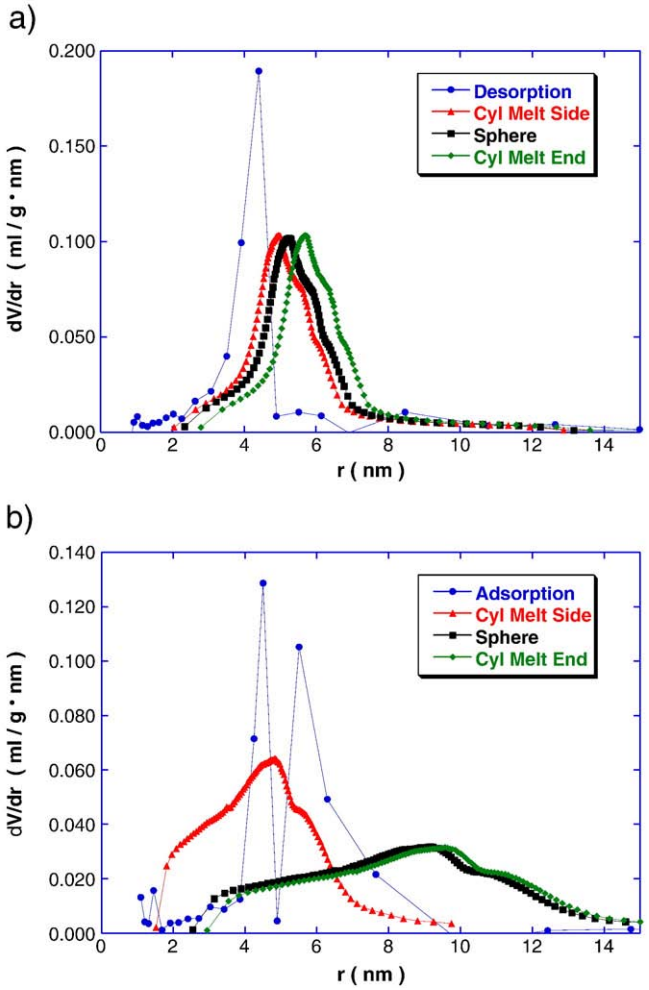


**Fig. 9.** Pore size distribution in Vycor® porous glass found from (a) nitrogen desorption and TPM freezing cycles; (b) nitrogen adsorption and TPM melting cycles. The pore liquid in TPM was pure water and the data were analyzed assuming that the pores are spherical (Sphere) or cylindrical with all melting from the side (Cyl Melt Side) or from the end (Cyl Melt End).

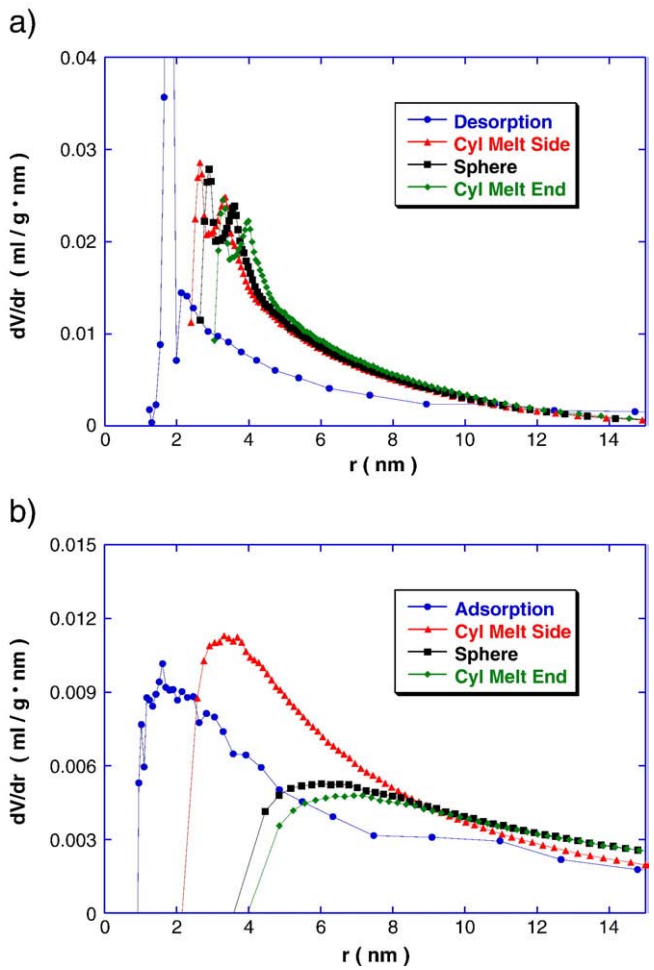


**Fig. 10.** Pore size distribution in mortar without entrained air, found from (a) nitrogen desorption and TPM freezing cycles; (b) nitrogen adsorption and TPM melting cycles. The pore liquid in TPM was limewater and the data were analyzed assuming that the pores are spherical (Sphere) or cylindrical with all melting from the side (Cyl Melt Side)

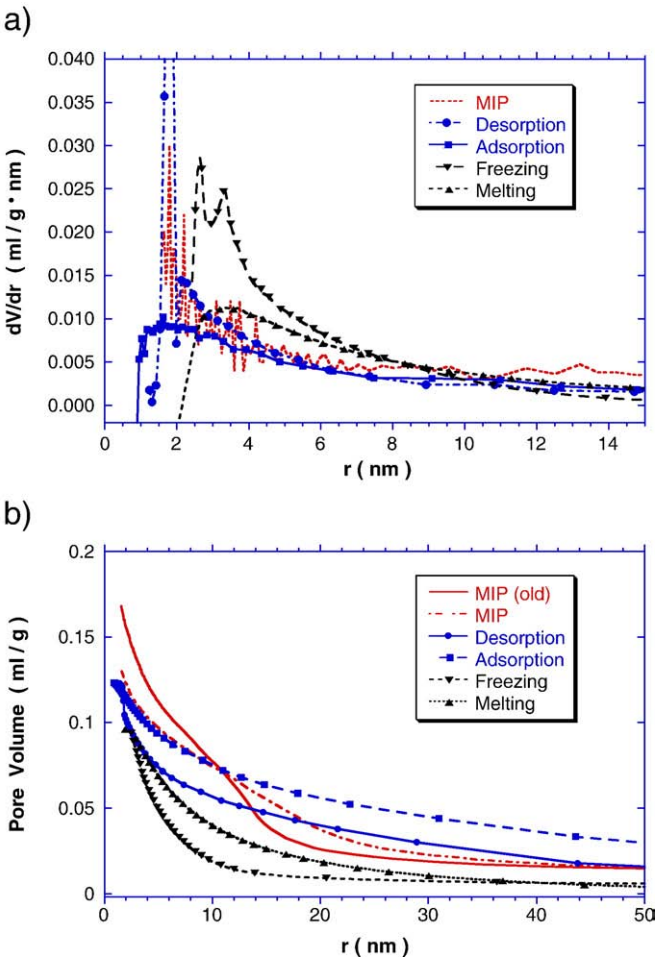


**Fig. 11.** Pore size distributions (a) and cumulative curves (b) measured by MIP, NAD, and TPM (assuming cylindrical pores, melting from the side) for a mortar without entrained air. The MIP curve labeled "old" was measured a year earlier, and the additional hydration time is seen to have reduced the pore volume and the proportion of pores with radii < 12 nm.

The pore size distribution from MIP is compared with those from NAD and TPM (assuming cylindrical pores melting from the side) in Fig. 11a. As expected, the MIP curve agrees with the nitrogen desorption curve. The smallest pores are not entered by ice, so the TPM curves lie slightly to right of the others. The cumulative curves in Fig. 11b give a different perspective: although the NAD curves show the steepest slope (so, the highest peak in the distribution curves) at radii < 5 nm, the cumulative curves show a higher volume of pores in the 10–40 nm range than either MIP or TPM. The MIP curve labeled "old" was measured shortly after the samples were received (at which point they had been hydrated for ~1.5 years); all the other samples were tested about a year later. The additional hydration time resulted in a reduction in pores with radii <12 nm and an increase in those with radii between 12 and 30 nm; the total pore volume decreased from 0.168 ml/g to 0.131 ml/g. (The density measurements described in the first paragraph of this section were made at a date midway between these MIP measurements.)

The mortar samples in the preceding figures had been dried and resaturated, so that their pore structure would be comparable to that of the dried samples used for NAD. The effect of drying and resaturating is shown in Fig. 12. As was shown by Villadsen [17], drying causes an increase in the size of the mesopores. In the present case, the median pore entry radius increases from about 4.6 nm before drying to 6.1 nm after drying.

## 5. Discussion

Based on a careful examination of the thermodynamic data and the physical assumptions employed, we conclude that the TPM analysis

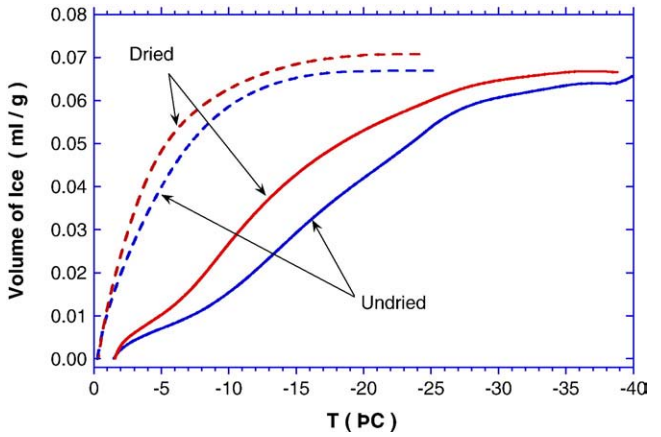


**Fig. 12.** Comparison of the freezing (solid) and melting (dashed) curves for a mortar that was not dried (Undried) and one that was exchanged into isopropanol, dried at 60 °C, and resaturated with water (Dried).

proposed by BLQE [27] is more accurate than others published more recently. The pore size distribution depends on the assumed pore shape and the mechanism of melting. For cylindrical pores, if melting occurred from the end, there would be very little hysteresis, whereas melting from the side would result in a twofold difference in the undercooling during freezing and melting. Since the observed hysteresis is always large, it appears that most cylindrical pores do melt from the side, as suggested by BLQE. However, since the data for porous glass yield $\lambda \approx 0.6$ for much of the temperature range, there must also be some pores that melt from the end, owing to network effects. Real pores will generally have interiors with radii larger than their entrances, so an alternative model, which provides a bound on the predicted pore size, is the spherical pore. In this case, the crystal/liquid interface is assumed to be spherical, so the curvature is $2/(r_E-\delta)$ during freezing and $2/(r_B-\delta)$ during melting. Contrary to the assertions of BLQE, we conclude that ice enters the pores by propagation, not by independent nucleation events; therefore, hysteresis is to be expected, even if the pore interiors are perfectly spherical, since $r_E<r_B$.

Comparison of the TPM results for porous glass containing pure water or water saturated with calcium hydroxide shows that there is a small increase in the thickness, $\delta$, of the unfrozen layer (see Table 3). This can be plausibly attributed to the presence of large hydrated cations in the unfrozen layer. Indeed, calcium ions cause a small, but measurable decrease in permeability of porous glass, apparently owing to a small increase in the thickness of the surface-affected layer [50]. However, $\delta$ is even larger in mortar, so there may be more ions in the pore liquid than is the case for Vycor®, or the structure or charge of the pore wall might be important. The present measurements indicate that the value $\delta = 0.8$ nm found by BLQE is a good estimate for water, but for cementitious materials containing limewater, we recommend using $\delta = 1.0$ nm with the cylindrical pore model or 1.2 nm with the spherical pore model.

## 6. Conclusions

Calorimetric data can be used directly to determine the pore shape parameter, $\lambda$, and the volume fraction of the pore space saturated with ice, without recourse to a model of pore shape. These results are used in a companion study [2] to predict the strain caused by crystallization of ice in the pores of mortar with and without air entrainment; the results are shown to be in good agreement with dilatometric measurements. Moreover, the shrinkage of the air entrained mortars is shown to account for the reduced scaling damage measured by Tremblay et al. [34] on these mortars.

For the analysis of pore shape by thermoporometry, we find that the method of analysis proposed by BLQE [27] is more reliable than others in the literature. In particular, the heat of fusion used in the analysis must be corrected for the effect of pressure in the liquid and for the contribution from interfacial energy. For pure water, the thickness of the unfrozen layer is $0.8 \pm 0.1$ nm, but it rises to 1.0–1.2 nm for limewater in mortar.

The pore sizes found for mortar by TPM are in reasonable agreement with those found by NAD. Neither of these techniques is accurate for measuring pores with radii larger than about 25 nm, but they are sensitive to the mesopores that control transport properties and crystallization pressure in cement paste. An advantage of TPM over NAD is that the samples do not need to be dried. Direct comparison of dried and undried samples shows that the pores in the latter are smaller.

## Acknowledgments

This work was supported by NSF Grant CMS-0509986. The authors are indebted to Marie-Hélène Tremblay and Jacques Marchand for providing the mortar samples used in this work.

## Appendix 1. Calculation of the baseline for DSC

Assuming that the instrument is calibrated such that the baseline without a sample is flat and equal to zero, the measured signal represents heat flow into the sample, $Q$ (mW) = d$h$/d$t$, where $h$ is heat (J) and $t$ is time. The heat capacity of the sample, $c_p$, is

$$mc_p = \frac{dh}{dT} = \frac{Q}{q} \tag{17}$$

where $m$ is the mass of the sample and $q = dT/dt$ is the heating rate. The reported heat flow is the sum of the baseline, $Q_B$, and the enthalpy of crystallization or melting, $Q_C$. In a plot of heat flow against time, the area under the curve is

$$h = \int Q\,dt \tag{18}$$

and the slope of the baseline is

$$\frac{dQ_B}{dt} = qm\frac{dc_p}{dt} \tag{19}$$

If the heat of fusion is $h_f$ (J/g), then the heat flow from crystallization or melting is

$$Q_C = h_f\frac{dm_C}{dt} \tag{20}$$

where $m_C$ is the mass of crystals in the pores.

The heat capacity includes contributions from the solid phase of the porous body, $c_{pS}$, the pore liquid, $c_{pL}$, and the crystals in the pores, $c_{pC}$:

$$mc_p = m_S c_{pS} + m_L c_{pL} + m_C c_{pC} \tag{21}$$

If the initial mass of the pore liquid is $m_{L0}$, then $m_L = m_{L0} - m_C$. The change in heat capacity of the sample results from the change in mass of crystals,

$$m\frac{dc_p}{dt} = (c_{pC}-c_{pL})\frac{dm_C}{dt} \tag{22}$$

Before the freezing peak, there will be a linear region where the heat flow is

$$Q_0 = Q_{B0} = qmc_{p0} = q(m_S c_{pS} + m_{L0} c_{pL}) \tag{23}$$

The location of the baseline at any later time is

$$Q_B(t) = Q_0 + \int_{t_0}^{t}\frac{dQ_B}{dt'}dt' = Q_0 + qmc_p(t) - qmc_p(t_0) = qmc_p(t) \tag{24}$$

so

$$Q_B(t) - Q_0 = qm(c_p - c_{p0}) = q(c_{pC}-c_{pL})m_C \tag{25}$$

The heat flow from crystallization is $Q_C$, so

$$Q(t) = Q_B + Q_C = Q_0 + q(c_{pC}-c_{pL})m_C + h_f\frac{dm_C}{dt} \tag{26}$$

or

$$\frac{dm_C}{dt} + \frac{q(c_{pC}-c_{pL})}{h_f} m_C = \frac{Q(t)-Q_0}{h_f} \tag{27}$$

Thus, the amount of ice formed at time $t$ is given by

$$m_C(t) = \int_{t_0}^{t} \exp\left[-\int_{t'}^{t} \frac{q(c_{pC}-c_{pL})}{h_f} dt''\right] \frac{Q(t')-Q_0}{h_f} dt' \tag{28}$$

or

$$m_C(T) = \int_{T_0}^{T} \exp\left[-\int_{T'}^{T} \frac{q(c_{pC}-c_{pL})}{q h_f} dT''\right] \frac{Q(T')-Q_0}{q h_f} dT' \tag{29}$$

If the experimental data are taken at a small temperature interval, $\Delta T$, we can expand this result using the trapezoidal rule to obtain

$$m_C(T+\Delta T) \approx m(T)x + \frac{\Delta T}{2}\left(\frac{Q(T)-Q_0}{q h_f}\right)x + \frac{\Delta T}{2}\left(\frac{Q(T+\Delta T)-Q_0}{q h_f}\right) \tag{30}$$

where

$$x \equiv \exp\left[-\frac{(c_{pC}-c_{pL})\Delta T}{q h_f}\right] \tag{31}$$

## Appendix 2. Correction for interfacial entropy

Brun et al. [27] apply a correction in their Eq. (9) that is derived by them in section F(c) of Ref. [41] (BLQE2). Their argument is reproduced here. They use a formulation due to Gibbs [51] and Guggenheim [52] in which the interface is treated as a separate phase with zero volume. First they consider the case of a bounding surface (subscript B) confining the liquid (L) and crystalline (C) phases, as in Fig. 13. The Gibbs–Duhem equations for a mole of the liquid and solid interphases are

$$d\mu_{LB} = -S_{LB}\,dT - A_{LB}\,d\gamma_{LB} \tag{32}$$

and

$$d\mu_{CB} = -S_{CB}\,dT - A_{CB}\,d\gamma_{CB} \tag{33}$$

where $S$ is the entropy, $A$ is the interfacial area, and $\gamma$ is the interfacial energy. At equilbrium, $d\mu_{LB} = d\mu_{CB}$, so

$$(S_{LB}-S_{CB})\,dT = -A_{LB}\,d\gamma_{LB} + A_{CB}\,d\gamma_{CB} \tag{34}$$

At this point, BLQE2 argue that the surface area covered by liquid or crystal would be about the same, $A = A_{LB} = A_{CB}$. This is a rough approximation, since those areas should be in the ratio of the molar volumes, $A_{LB}/A_{CB} = V_L/V_C$ , but it allows them to make use of Young's equation,

$$\gamma_{LB} = \gamma_{CB} - \gamma_{CL}\cos(\theta) \tag{35}$$

where $\theta$ is the contact angle made by the crystal with the boundary; the negative sign results from the unorthodox definition of $\theta$ in Fig. 13a. The result of substituting Eq. (35) into Eq. (34) is

$$(S_{LB}-S_{CB})\,dT = -A\,d(\gamma_{LB}-\gamma_{CB}) = A\,d\gamma_{CL}\cos(\theta) \tag{36}$$

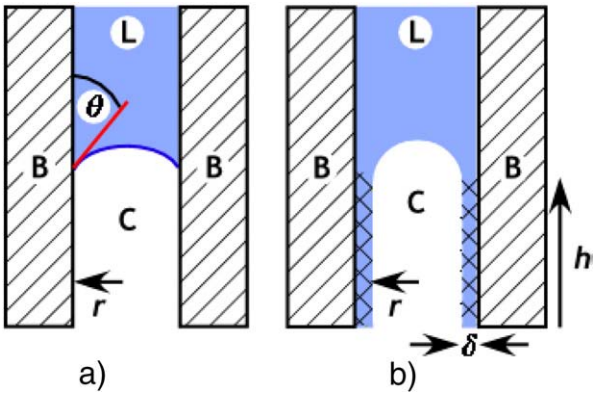


**Fig. 13.** Sketch of pore, after Ref. [41], where B is the boundary (confining) phase, C is the crystal, and L the liquid. In (a), the crystal is in contact with the boundary, and has a contact angle of $\theta$. In (b), there is an interfacial layer (cross-hatched) with thickness $\delta$. The radius of the crystal is $r$ and the length in contact with the boundary is $h$.

In a pore of radius $r$, suppose that a mole of interphase covers an area $A = 2\pi r h$; that length of pore will contain a number of moles, $n$, equal to $\pi r^2 h/V_L$. Thus, $A = 2nV_L/r$ and the "superficial" entropy associated with the freezing of that amount of liquid is

$$\Delta S_{f\,\mathrm{sup}} \equiv S_{LB} - S_{CB} = \frac{2nV_L}{r}\frac{d\gamma_{CL}}{dT}\cos(\theta) \tag{37}$$

If the boundary is an unfrozen layer, as in Fig. 13b, BLQE2 point out that the preceding equations still apply, but B represents the unfrozen interfacial layer with thickness $\delta$.

Departing from the approach of BLQE2, we can argue that the energy of the interface between the pore liquid and the unfrozen layer, $\gamma_{LI}$ , should be small, since they are the same liquid with slightly modified structure. If so, Eqs. (34) and (35) can be approximated by

$$(S_{LI}-S_{CI})\,dT \approx A_{CI}\,d\gamma_{CI} \tag{38}$$

and

$$\gamma_{CI} \approx \gamma_{CL}\cos(\theta) \approx \gamma_{CL} \tag{39}$$

and Eq. (37) becomes

$$\Delta S_{f\,\mathrm{sup}} = S_{LI} - S_{CI} \approx A_{CI}\frac{d\gamma_{CL}}{dT} \approx \frac{2nV_C}{r}\frac{d\gamma_{CL}}{dT} \tag{40}$$

In this case, $r$ is the radius of the ice (represented by $R_n$ in BLQE, and by $r_{CL}$ in the present paper). Eq. (40) is the same as the result of BLQE2, within the bounds of their approximation, $A_{LB} = A_{CB}$, which implies that $V_L \approx V_C$.

In Ref. [27], BLQE work in terms of energy per gram, so we must divide Eq. (40) by $n$ times the molecular weight, which yields,

$$\Delta S_{f\,\mathrm{sup}}\,(\mathrm{J/g}) \approx \frac{2v_C}{r}\frac{d\gamma_{CL}}{dT} \tag{41}$$

where $v_C$ is the specific volume of the crystalline phase. The sign of this result is different from that in eq. (9) of BLQE, because that equation applies to freezing, whereas Eq. (41) describes the entropy increase upon melting. To replace $r$ with a function of temperature, BLQE make use of Eq. (13). During the freezing cycle, $r = r_p - \delta$, so when the pore liquid is water, the radius of the crystal is related to the undercooling by

$$r = r_{CL}(\mathrm{nm}) \approx \frac{64.67}{\Delta T} - 0.23 \tag{42}$$

During the melting cycle, at the same $\Delta T$, the curvature of the ice crystal is half as large, so

$$r \approx \frac{32.33}{\Delta T} - 0.11 \tag{43}$$

Substituting Eq. (42) or (43) into Eq. (41), and using Eq. (12) to find $d\gamma_{CL}/dT$ leads to Eqs. (7) and (8), respectively.

If the pores are assumed to be spherical, then this analysis must be modified. If we proceed analogously, assuming that the area of the interface is $A_{CI} = 4\,\pi\,r^2$ and the number of moles of ice in the pore is $n = 4\,\pi\,r^3/(3\,V_L)$, we will arrive at Eq. (41) with the factor of 2 changed to 3. However, this would be valid only during melting in a pore that is nearly a complete sphere; such a pore would necessarily have an entry radius much smaller than that of the interior. If ice enters the spherical pore through a small opening, as suggested in Fig. 4, then the freezing temperature is controlled by the radius of the entry, not the interior. Using the radius of the entry would lead to an overestimate of the surface-to-volume ratio of the ice inside the pore. There is no simple resolution to this problem, so we will proceed as in BLQE, using Eqs. (41) and (42) to describe both the melting and freezing curves for the spherical pore model. The overestimate of the interfacial area is partially offset by using a factor of 2, rather than 3, in Eq. (41). For a spherical pore with interior radius $R_i$ and two entries with radius $R_e$, the surface-to-volume ratio can be shown to be $s = 6R_i/(2R_i^2 + R_e^2)$, whereas that implied by Eq. (41) is $s' = 2/R_e$ . The error resulting from use of the latter is < 10% if $R_e/R_i > 0.8$, but it rises to > 50% if $R_e/R_i < 0.5$. (Of course, a typical pore will have more than two entries, so these are only crude estimates.) Therefore, it is prudent to test Eq. (41) for spherical pores, but to distrust the results if the analysis indicates that $R_e/R_i < 0.8$.

An iterative scheme can be used to adjust the entropy correction for the spherical model; however, the errors resulting from our ignorance of pore connectivity (as discussed in connection with Fig. 2) make such refinements pointless. Therefore, following BLQE, we will simply use Eqs. (41)–(43) and accept the uncertainty in the pore size distribution.

## References


[1] G.W. Scherer, J.J. Valenza II, Mechanisms of Frost Damage, in: J. Skalny, F. Young (Eds.), Materials Science of Concrete, vol. VII, American Ceramic Society, 2005, pp. 209–246.
[2] Z. Sun and G.W. Scherer, Effect of air voids on salt scaling, Cement Concr. Res. (in press)
[3] H.M. Jennings, Refinements to colloid model of C-S-H in cement: CM-II, Cem. Concr. Res. 38 (2008) 275–289.
[4] T.C. Powers, T.L. Brownyard, Studies of the physical properties of hardened Portland cement paste. Part 2. Studies of water fixation, J. Am. Concr. Inst. 18 (3) (1946) 249–303.
[5] T.C. Powers, The air requirement of frost-resistant concrete, Proc. Highway Res. Board 29 (1949) 184–211.
[6] M. Pigeon, R. Pleau, Durability of Concrete in Cold Climates, E & FN Spon, London, 1995.
[7] S.H. Kosmatka, W.C. Panarese, Design and Control of Concrete Mixtures, 13th ed. Portland Cement Association, Skokie, IL, 1988 Ch. 8.
[8] R.F. Feldman, The porosity and pore structure of hydrated Portland cement paste, in: L.R. Roberts, J.P. Skalny (Eds.), Pore Structure and Permeability of Cementitious Materials, vol. 137, Materials Research Society, Pittsburgh, PA, 1989, pp. 59–73.
[9] J.J. Thomas, H.M. Jennings, A.J. Allen, The surface area of hardened cement paste as measured by various techniques, Concr. Sci. Eng. 1 (1999) 45–64.
[10] G.W. Scherer, J.J. Valenza II, G. Simmons, New methods to measure liquid permeability in porous materials, Cem. Concr. Res. 37 (2007) 386–397.
[11] S.J. Gregg, K.S.W. Sing, Adsorption, Surface Area and Porosity, 2nd ed. Academic, London, 1982.
[12] S. Diamond, Mercury porosimetry: an inappropriate method for the measurement of pore size distributions in cement-based materials, Cem. Concr. Res. 30 (2000) 1517–1525.
[13] K.L. Scrivener, The use of backscattered electron microscopy and image analysis to study the porosity of cement paste, in: L.R. Roberts, J.P. Skalny (Eds.), Pore Structure and Permeability of Cementitious Materials, vol. 137, Materials Research Society, Pittsburgh, PA, 1989, pp. 129–140.
[14] T.C. Powers, L.E. Copeland, J.C. Hayes, H.M. Mann, Permeability of Portland Cement Paste, Bull., Portland Cem. Assoc. 53 (1955) 285–298.
[15] D.H. Bager, E.J. Sellevold, Ice formation in hardened cement paste, Part III—Slow resaturation of room temperature cured pastes, Cem. Concr. Res. 17 (1987) l–ll.
[16] R.M. Espinosa, L. Franke, Influence of the age and drying process on pore structure and sorption isotherms of hardened cement paste, Cem. Concr. Res. 36 (2006) 1969–1984.
[17] J. Villadsen, Pore structure in cement based materials, Tech. Rep. 277, Building Materials Lab., Technical Univ., Denmark, 1992, ISSN 0908-3871.
[18] W.P. Halperin, F. D'Orazio, S. Bhattacharja, J.C. Tarczon, Magnetic resonance relaxation analysis of porous media, in: J. Klafter, J.M. Drake (Eds.), Molecular Dynamics in Restricted Geomtries, Wiley, New York, 1989, pp. 311–350.
[19] W.P. Halperin, J.-Y. Jehng, Y.-Q. Song, Application of spin–spin relaxation to measurement of surface area and pore size distributions in a hydrating cement paste, Magn. Reson. Imaging 12 (1994) 169–173.
[20] J. Mitchell, J. Beau, W. Webber, J.H. Strange, Nuclear magnetic resonance cryoporometry, Phys. Rep. 461 (2008) 1–36.
[21] J.-Y. Jehng, D.T. Sprague, W.P. Halperin, Pore structure of hydrating cement paste by magnetic resonance relaxation analysis and freezing, Magn. Reson. Imaging 14 (7/8) (1996) 785–791.
[22] G.W. Scherer, D.M. Smith, D. Stein, Deformation of aerogels during characterization, J. Non-Cryst. Solids 186 (1995) 309–315.
[23] A.M. Kjeldsen, M.R. Geiker, On the interpretation of low temperature calorimetry data, Mater. Struct. 41 (2008) 213–224.
[24] R. Defay, I. Prigogine, Surface Tension and Adsorption, Wiley, New York, 1966.
[25] W. Kuhn, E. Peterli, H. Majer, Freezing point depression of gels produced by high polymer network, J. Polym. Sci. 16 (1955) 539–548.
[26] G. Fagerlund, Determination of pore-size distribution from freezing-point depression, Mater. Struct. 6 (33) (1973) 215–225.
[27] M. Brun, A. Lallemand, J.F. Quinson, C. Eyraud, A new method for the simultaneous determination of the size and the shape of pores: the thermoporometry, Thermochim. Acta 21 (1977) 59–88.
[28] H.F.W. Taylor, Cement Chemistry, 2nd ed. Thomas Telford, London, 1997.
[29] T.C. Powers, T.L. Brownyard, Studies of the physical properties of hardened Portland cement paste. Part 8. The freezing of water in hardened Portland cement paste, J. Am. Concr. Inst. 18 (8) (1947) 933–969.
[30] J.F. Quinson, M. Brun, "Transformations de phase liquide–solide des solutions salines retenues au sein d'un milieu poreux: cas ou le materiau est sature en eutectique", [Liquid–solid phase transformations of salt solutions within porous media: case of a material saturated with a eutectic composition], J. Chim. Phys. 81 (10) (1984) 611–615.
[31] J.W. Christian, The Theory of Transformations in Metals and Alloys, Part I, Pergamon, New York, 1975.
[32] G.W. Scherer, Freezing gels, J. Non-Cryst. Solids 155 (1993) 1–25.
[33] D.H. Rasmussen, A.P. MacKenzie, Clustering in supercooled water, J. Chem. Phys. 59 (9) (1973) 5003–5013.
[34] M.-H. Tremblay, F. Lory, J. Marchand, G.W. Scherer, J.J. Valenza, Ability of the glue spall model to account for the de-icer salt scaling deterioration of concrete, paper W4-07.3, in: J.J. Beaudoin, J.M. Makar, L. Raki (Eds.), Proc. 12th ICCC, National Research Council of Canada, Montreal, Canada, ISBN: 978-0-660-19695-4, 2007.
[35] N.C. Collier, J.H. Sharp, N.B. Milestone, J. Hill, I.H. Godfrey, The influence of water removal techniques on the composition and microstructure of hardened cement pastes, Cem. Concr. Res. 38 (2008) 737–744.
[36] S. Ghabezloo, J. Sulem, S. Guédon, F. Martineau, J. Saint-Marc, Poromechanical behaviour of hardened cement paste under isotropic loading, Cem. Concr. Res. 38 (12) (2008) 1424–1437.
[37] R.A. Olson, C.M. Neubauer, H.M. Jennings, Damage to the pore structure of hardened Portland cement paste by mercury intrusion, J. Am. Ceram. Soc. 80 (9) (1997) 2454–2458.
[38] K. Ishikiriyama, M. Todoki, K. Motomura, Pore size distribution (PSD) measurements of silica gels by means of differential scanning calorimetry I. Optimization for determination of PSD, J. Colloid Interface Sci. 171 (1995) 92–102.
[39] K. Ishikiriyama, M. Todoki, Pore size distribution measurements of silica gels by means of differential scanning calorimetry II. Thermoporosimetry, J. Colloid Interface Sci. 171 (1995) 103–111.
[40] M.R. Landry, Thermoporometry by differential scanning calorimetry: experimental considerations and applications, Thermochim. Acta 433 (2005) 27–50.
[41] M. Brun, A. Lallemand, J.F. Quinson, C. Eyraud, Changement d'état liquid–solide dans les milieux poreux. II. Étude théorique de la solidification d'un condensat capillaire, (Liquid–solid change of state in porous media. II. Theoretical study of the solidification of a capillary condensate), J. Chim. Phys. 6 (1973) 979–989.
[42] David R. Lide (Ed.), CRC Handbook of Chemistry and Physics, 83 rd ed., CRC Press, Boca Raton, FL, 2002, p. 6-6.
[43] A. Skapski, R. Billups, A. Rooney, Capillary cone method for determination of surface tension of solids, J. Chem. Phys. 26 (5) (1957) 1350–1351.
[44] W.M. Ketcham, P.V. Hobbs, An experimental determination of the surface energies of ice, Phil. Mag. 19 (162) (1969) 1161–1173.
[45] M. Dunn, J.C. Dore, P. Chieux, Structural studies of ice formation in porous silicas by neutron diffraction, J. Cryst. Growth 92 (1988) 233–238.
[46] M.-C. Bellissent-Funel, J. Lal, L. Bosio, Structural study of water confined in porous glass by neutron scattering, J. Chem. Phys. 98 (5) (1993) 4246–4252.
[47] Y.P. Handa, M. Zakrzewski, C. Fairbridge, Effect of restricted geometries on the structure and thermodynamic properties of ice, J. Phys. Chem. 96 (1992) 8594–8599.
[48] E.M. Schulson, I.P. Swainson, Thomas M. Holden, Charles J. Korhonen, Hexagonal ice in hardened cement, Cem. Concr. Res. 30 (2000) 191–196.
[49] J.A. Dean (Ed.), Lange's Handbook of Chemistry, McGraw-Hill, New York, 1973.
[50] S. Xu, G.C. Simmons, T.S. Mahadevan, G.W. Scherer, S.H. Garofalini, Carlos Pacheco, Transport of Water in Small Pores, Langmuir 25 (9) (2009) 5084–5090.
[51] J.W. Gibbs, Collected Works, Longmans Green & Co., New York, 1928.
[52] E.A. Guggenheim, Thermodynamique, Dunod, Paris, 1965.